Porous Carbon Catalysts

DOI: 10.1002/anie.201307319

Nitrogen-Doped Carbon Nanosheets with Size-Defined Mesopores as Highly Efficient Metal-Free Catalyst for the Oxygen Reduction Reaction**

Wei Wei, Haiwei Liang, Khaled Parvez, Xiaodong Zhuang, Xinliang Feng, and Klaus Müllen**

Abstract: *Nitrogen-doped carbon nanosheets (NDCN) with size-defined mesopores are reported as highly efficient metal-free catalyst for the oxygen reduction reaction (ORR). A uniform and tunable mesoporous structure of NDCN is prepared using a templating approach. Such controlled mesoporous structure in the NDCN exerts an essential influence on the electrocatalytic performance in both alkaline and acidic media for the ORR. The NDCN catalyst with a pore diameter of 22 nm exhibits a more positive ORR onset potential than that of Pt/C (−0.01 V vs. −0.02 V) and a high diffusion-limited current approaching that of Pt/C (5.45 vs. 5.78 mA cm^{-2}) in alkaline medium. Moreover, the catalyst shows pronounced electrocatalytic activity and long-term stability towards the ORR under acidic conditions. The unique planar mesoporous shells of the NDCN provide exposed highly electroactive and stable catalytic sites, which boost the electrocatalytic activity of metal-free NDCN catalyst.*

Efficient catalysts for the oxygen reduction reaction (ORR) are considered the key to achieve optimal performance for fuel cells and metal–air batteries.[1] The catalysts of choice for the desired four-electron transfer ORR process are platinum and its alloys;[1] however, their sluggish kinetics, vulnerability, and the scarcity of platinum impede the development and commercialization of fuel cells.[2] In this regard, much effort has been devoted to the search for substitutes for platinum catalysts by employing nonprecious metal catalysts,[3] or metal-free heteroatom-enriched (e.g. N, B, and S) carbonaceous materials.[4] Incorporation of heteroatoms within a carbonaceous skeleton can effectively modulate the catalytic sites, chemisorption energy of O_2, and the reaction mechanism ($2e^-/4e^-$) of catalysts, leading to significant enhancement in the ORR performance.[5] Nitrogen-doped carbon materials (NCMs) represent the most investigated catalysts for the ORR because they not only exhibit excellent electrocatalytic activity but also possess other advantages, including low costs, long durability, and environmental friendliness.[6,7] The critical feature related to the ORR activity of NCMs is the charge delocalization of the carbon atoms induced by nitrogen doping, which results in the non-electroneutrality of the catalysts and consequently facilitates oxygen adsorption and reduction.[8] Moreover, the ORR performance of NCMs is also strongly governed by parameters such as the atomic ratio of different types of nitrogen atoms (graphitic and pyridinic N atoms), surface area, and the degree of sp^2 bonding in the carbon framework.[9]

Graphene, a two-dimensional (2D) monolayer sheet of hexagonal carbon, exhibits intriguing properties such as high surface area, superior electrical conductivity, and excellent mechanical/chemical stability.[10] Its unique planar structure renders graphene a suitable substrate for creating hybrids containing numerous catalytic sites with the promise of efficient transport pathways.[4c,8a,9c] Morphology control over graphene associated with heteroatom doping has been demonstrated to effectively promote the activity of NCMs for the ORR in alkaline electrolyte.[11] However, metal-free NCM catalysts suffer from low activity in acidic media, mostly because of the relatively few catalytic sites within these catalysts.[12]

Here, we developed a series of nitrogen-doped carbon nanosheets (NDCN) with uniform and tuneable mesopores. Porosity control over NDCN is achieved by employing an appropriate graphene/silica nanosheet template that is built up by the direct growth of mesoporous silica and the electrostatic assembly of colloidal silica nanoparticles (NPs) of different sizes on a graphene oxide (GO) surface. Surface coating of polydopamine (PDA) followed by pyrolysis and removal of the silica template yield NDCN with size-defined mesopores which have exposed highly electroactive and stable catalytic sites (graphitic and pyridinic N atoms).

Remarkably, the NDCN shows a close relationship between the electrocatalytic activity and the pore size. NDCN with a mesopore size of about 22 nm exhibits the highest ORR performance, with a well-defined plateaux for the diffusion-limiting current and a more positive onset potential than that of a Pt/C catalyst in an alkaline medium (−0.01 V vs. −0.02 V). Moreover, the NDCN catalyst manifests pronounced catalytic activity in acidic medium, with mainly a 4-electron transfer process, an ORR onset potential of 0.72 V versus the reversible hydrogen electrode (RHE), and a high current density of 3.57 mA cm^{-2} at 0.50 V. To the best of our knowledge, such excellent electrochemical per-

[*] W. Wei, Dr. H. Liang, K. Parvez, Prof. X. Feng, Prof. K. Müllen
Max Planck Institute for Polymer Research
Ackermannweg 10, 55128 Mainz (Germany)
E-mail: feng@mpip-mainz.mpg.de
muellen@mpip-mainz.mpg.de
Dr. X. Zhuang, Prof. X. Feng
School of Chemistry and Chemical Engineering
Shanghai Jiao Tong University, Shanghai 200240 (P. R. China)

[**] This work was financially supported by the ERC grants for NANOGRAPH and 2DMATER, the DFG Priority Program SPP 1459, the ESF Project GOSPEL (grant number 9-EuroGRAPHENE-FP-001), the EC under the Graphene Flagship (grant number CNECT-ICT-604391), the EU GENIUS, UPGRADE, and MOLESOL Projects. The authors thank Dr. Rongjin Li for helpful discussions.

Supporting information for this article is available on the WWW under http://dx.doi.org/10.1002/anie.201307319.

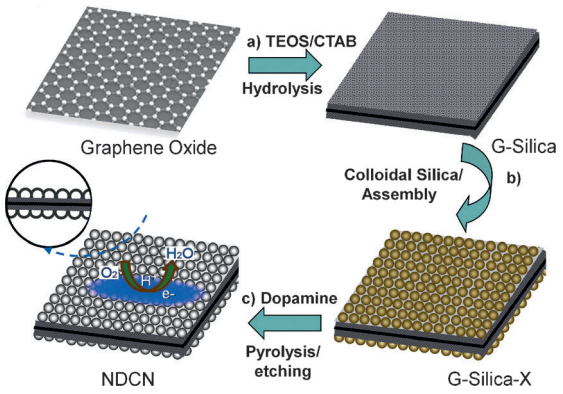

Figure 1. Synthesis of NDCN-X. a) CTAB-directed hydrolysis of TEOS on GO nanosheets (CTAB = cetyltrimethyl ammonium bromide, TEOS = tetraethylorthosilicate, and GO = graphene oxide). b) Electrostatic assembly of G-silica and colloidal silica NPs. c) Self-polymerization of DA, pyrolysis, and silica removal treatment (DA = dopamine).

formance in both alkaline and acidic media for the ORR has not been achieved for metal-free carbon catalysts.

The overall synthetic procedure for the NDCN is presented in Figure 1 and in Figure S1a in the Supporting Information. A mesoporous silica shell was initially grown on GO using cetyltrimethyl ammonium bromide (CTAB) -directed hydrolysis of tetraethylorthosilicate (TEOS), to generate graphene-based silica nanosheets (G-silica) with a mesopore size of 2 nm.[13] G-silica was then functionalized with polydiallyldimethylammonium chloride (PDDA-functionalized G-silica), and electrostatically assembled with negatively charged colloidal silica NPs in aqueous solution. As a result, G-silica was further sandwiched with shells comprising close-packed colloidal silica NPs (denoted G-silica-X, where X represents the particle size of colloidal silica NPs or the pore size of the resultant NDCN). Afterwards, G-silica-X was dispersed in an aqueous solution of dopamine (DA), and homogeneous PDA layers were readily coated onto the surface of G-silica-X by the self-polymerization of DA under ambient conditions.[14] The subsequent thermal treatment of PDA-coated G-silica-X in nitrogen combined with etching of silica generated NDCN-X with defined mesopores. Thereby, for the first time, successful control of porosity over the NDCN was realized by employing colloidal silica with different particle sizes.

To achieve a favorable electrostatic assembly between G-silica and colloidal silica NPs, the surface charges of colloidal silica NPs and G-silica before and after functionalization with PDDA depending on various pH values were monitored by zeta potential measurements (Figure 2a). Typically, the surface charge of silica-22 and pristine G-silica are negative over the entire investigated pH range (1–12). As expected, the surface charge of PDDA-functionalized G-silica is positive over the pH range from 1 to 12, in contrast to that of pristine G-silica. Therefore, assembly between G-silica and silica-22 was carried out using electrostatic interactions at an optimal pH value of around 5, where a broad zeta potential gap (dashed line in Figure 2a) between PDDA-functionalized G-

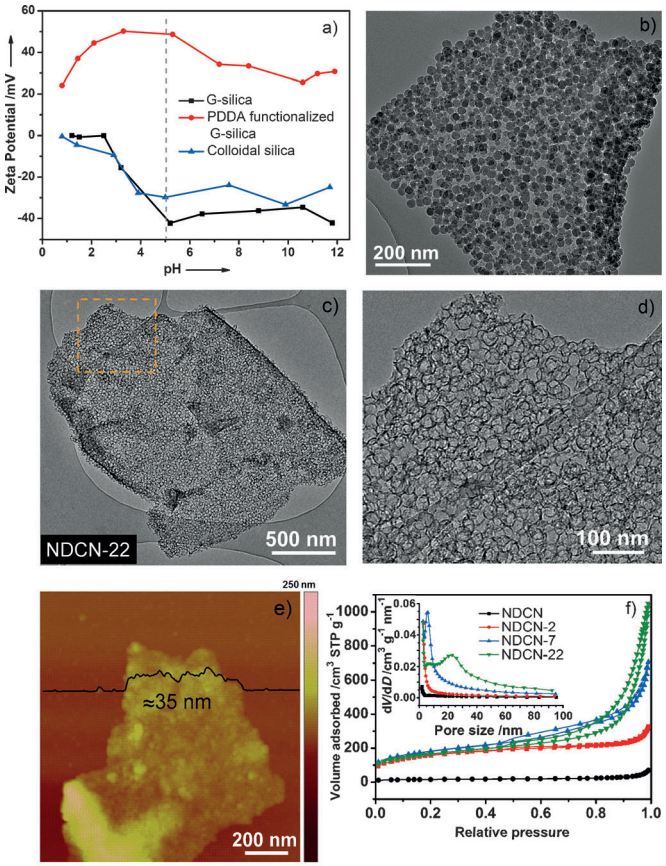

Figure 2. a) Zeta potentials of silica-22, and G-silica before and after functionalization with PDDA under different pH conditions. b) Typical TEM image of G-silica-22, revealing the uniform adhesion of silica-22 on the surface of G-silica. c) Morphology and microstructure of the resulting NDCN-22; image d) is of the square region marked in (c). e) Representative AFM image of NDCN-22 and the corresponding thickness analysis taken around the black line. f) Nitrogen adsorption/desorption isotherms and BJH pore distributions (inset) of the NDCN and NDCN-X.

silica and silica-22 creates strong mutual interactions.[15] TEM measurement verified the successful fabrication of G-silica-22 (Figure 2b and Figures S1b and S1c). Notably, neither free silica-22 nor bare areas of G-silica were observed. For comparison, silica-22 was mixed with pristine G-silica without PDDA functionalization. It was found that most of the silica-22 was randomly distributed around the G-silica instead of uniform coating (Figure S1d), thus validating the electrostatic interaction as the crucial driving force of the assembly. Such an assembly approach was conveniently extended to fabricate G-silica-7 by employing colloidal silica NPs with a diameter of about 7 nm (silica-7, Figure S2a and S2b).

Gentle stirring of G-silica-22 and G-silica-7 in aqueous DA solution (buffered to pH 8.5 with Tris) resulted in the spontaneous coating of adherent PDA layers (Figure S3a and S3c). The thickness of the PDA coating layer could be adjusted by the polymerization time, which was elucidated by the thickness variation of carbon layers (see Figure S4). PDA-wrapped G-silica-22 or G-silica-7 was then placed in a tube furnace for carbonization at 900 °C in nitrogen atmosphere.

The carbon layer was continuous without any cracks after thermal treatment, as shown in Figure S3b and S3d. The morphology and microstructure of NDCN-22 and NDCN-7 after etching of silica were characterized by TEM (Figure 2c,d and Figure S2c, S2e, and S2f). Both sides of NDCN-22 and NDCN-7 were decorated with uniform and size-defined mesopores; the mesopores were interconnected on the surface of the NDCN to form 2D planar mesoporous shells. High-resolution TEM revealed that the carbon layer obtained was less than 5 nm in thickness (Figure S2d). Further, control experiments of PDA coating were conducted on pristine graphene nanosheets and G-silica to produce NDCN and NDCN-2. The typical atomic force microscopy (AFM) image and thickness analyses of NDCN-22, shown in Figure 2e, reveal a 2D porous feature with an average thickness of 35 nm. In the Raman spectra of NDCN and NDCN-X nanosheets (Figure S6a), two peaks emerge near 1590 cm^{-1} and 1352 cm^{-1}, which can be assigned to the G (graphitic carbon) and D bands (disordered carbon), respectively. The I_D/I_G values disclose a similar graphitic nature for all of the prepared samples.

The porous features and Brunauer–Emmett–Teller (BET) specific surface areas of the NDCN and NDCN-X were investigated by nitrogen isothermal adsorption/desorption measurements (Figure 2f). The BET specific surface areas for NDCN-2, NDCN-7, and NDCN-22 were calculated to be 578, 652, and 589 m^2g^{-1}, respectively, which are much higher than that of NDCN (55 m^2g^{-1}). Notably, upon increasing the pore size of NDCN-X, the pore volume significantly increased from 0.38 m^3g^{-1} for NDCN-2 to 1.52 m^3g^{-1} for NDCN-22. The steep increase in nitrogen adsorption for NDCN-22 and NDCN-7 at a relatively high pressure ($P/P_0 = 0.80$–0.99) clearly suggests that the pore volume is mainly contributed by size-enlarged mesopores.[16] Based on the Barrett–Joyner–Halenda model (BJH model; inset of Figure 2f), the pore size distribution calculated from the adsorption branch reveals the mesoporous feature for all NDCN-X samples. Moreover, NDCN-22 and NDCN-7 exhibit a mesopore distribution peak at 22 and 7 nm, respectively, consistent with the diameter of the silica-22 and silica-7 template. In contrast, no evident mesopores were observed for the NDCN. X-ray photoelectron spectroscopy (XPS) measurements were carried out to probe the chemical composition of all materials. The survey scan spectra from the XPS analysis show the presence of C1s, O1s, and N1s signals (Figure S6b). The atomic content is summarized in Table S1. As expected, the NDCN and NDCN-X showed a high content of carbon (above 87.7 at%.) and doped nitrogen with a narrow content distribution (3.2–3.7 at%). Typically, NDCN-22 had an atomic content of 89.2, 7.3, and 3.5% for carbon, oxygen, and nitrogen, respectively (Figure S6c). The complex N1s spectrum could be further deconvoluted into three signals with binding energies of 398.5, 401.0, and 402.4 eV that correspond to pyridinic N atoms(35.4 at%), graphitic N atoms (55.0 at%) and pyridinic N^+-O^- groups (9.6 at%), respectively (Figure S6d).[17,3c]

The electrocatalytic activity of NDCN-X for the ORR was first examined by cyclic voltammetry (CV) in an Ar- or O_2-saturated 0.1M KOH solution at a scan rate of 100 $mV s^{-1}$. As

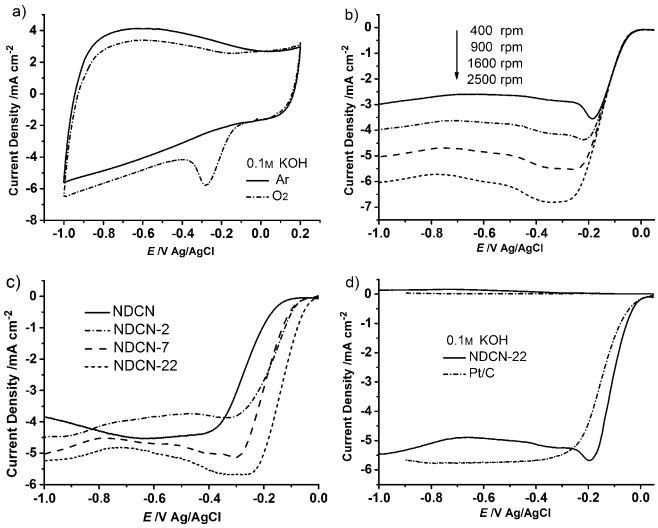

Figure 3. a) CV of NDCN-22 in Ar- and O_2-saturated 0.1 M KOH solution at a scan rate of 100 $mV s^{-1}$. b) linear sweep voltammetry (LSV) of NDCN-22 in O_2-saturated 0.1 M KOH at a scan rate of 10 $mV s^{-1}$ at different RDE rotation rates. c) LSV of the NDCN and NDCN-X in O_2-saturated 0.1 M KOH at a scan rate of 10 $mV s^{-1}$ with an RDE rotation rate of 1600 rpm. d) RRDE polarization curves for NDCN-22 and Pt/C in O_2-saturated 0.1 M KOH at a scan rate of 10 $mV s^{-1}$ with an RDE rotation rate of 1600 rpm. For all the rotating disk electrode (RDE) and the rotating ring-disk electrode (RRDE) measurements, the loading of catalysts was 20 $\mu g_{Pt} cm^{-2}$ for Pt/C and 0.6 $mg cm^{-2}$ for NDCN-X and the NDCN.

shown in Figure 3a, a quasi-rectangular voltammogram without any obvious peak was observed for NDCN-22 in the Ar-saturated solution. In contrast, a well-defined cathodic ORR peak, centered at −0.28 V with a high reaction current of $-5.8\ mA cm^{-2}$ occurred in the CV analysis when the electrolyte solution was saturated with O_2, highlighting pronounced electrocatalytic activity of NDCN-22 for oxygen reduction. To gain insight into the reaction kinetics of NDCN-22, linear sweep voltammetry (LSV) with a rotating disk electrode (RDE) was undertaken at different rotating speeds from 400 to 2500 rpm in an O_2-saturated 0.1M KOH solution (Figure 3b). NDCN-22 showed a well-defined plateaux of diffusion-limiting currents below −0.3 V at all rotational speeds, indicating an efficient surface electrocatalytic reaction with a direct four-electron transfer pathway. We further used the RDE to probe the pore size effect on the ORR catalytic activity of different catalysts. The LSV results for NDCN and NDCN-X are presented in Figure 3c. Notably, the onset potential of all NDCN-X catalysts is more positive than that of the NDCN. In particular, NDCN-22 exhibited the most positive half-wave potential ($E_{1/2}$) and the highest kinetic current density compared with its counterparts (see Table S2). This result thus strongly suggests that the controlled mesoporous structure in the NDCN-X exerts an essential influence on the electrocatalytic behavior.

To assess the electrocatalytic activity of NDCN-X, rotating ring-disk electrode (RRDE) measurements were also carried out on NDCN-22 and commercial Pt/C (20 wt%) in O_2-saturated 0.1M KOH at a rotation rate of 1600 rpm (Figure 3d). Remarkably, NDCN-22 exhibited a diffusion-

limiting current approaching that of Pt/C (5.45 vs. 5.78 mA cm^{-2}), and even a more positive onset and half-wave potential (−0.01 and −0.11 V) than those of Pt/C (−0.02 and −0.15 V). To the best of our knowledge, these values including the onset/half-wave potential and the diffusion-limiting current are superior to other NCMs reported to date as metal-free ORR catalysts in an alkaline medium (see Table S3). The slight decrease in the current density at the overpotential of about −0.2 V might be caused by the rapid O_2 consumption in the test cells. On the basis of the ring and disk currents, the electron transfer number (n) for NDCN-22 is calculated to be 3.67–3.94 over the potential range from −0.2 to −0.9 V (Figure S7a), emphasizing that NDCN-22 proceeds mainly by a four-electron ORR mechanism.

Next, the effect of the mesopore size characteristics on electrocatalytic performance in acidic medium was investigated. The CV curve indicated a significant reduction process for NDCN-22, with a pronounced cathodic ORR peak at 0.50 V versus the reversible hydrogen electrode (RHE) when the electrolyte (0.5 M H_2SO_4) was saturated with O_2 (Figure 4a). The RDE polarization curves of NDCN and NDCN-X (Figure S7b) indicated that the onset and half-wave

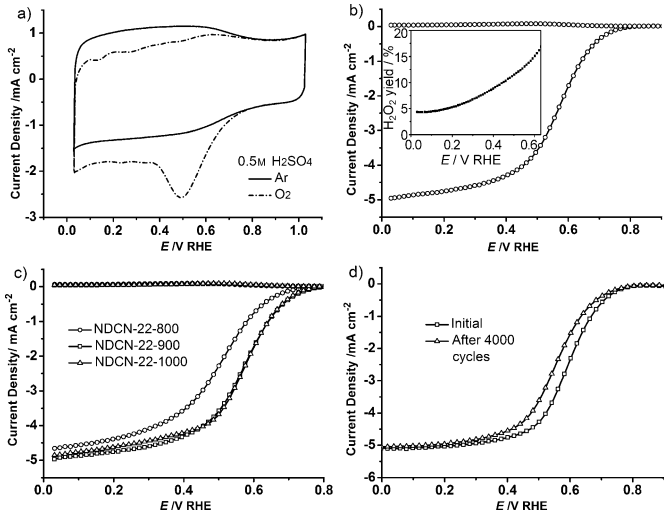

Figure 4. a) CV of NDCN-22 in Ar- and O_2-saturated 0.5 M H_2SO_4 solution at a scan rate of 100 mV s^{-1}. b) The RRDE voltammetric response and H_2O_2 yield plot (inset) of NDCN-22 in O_2-saturated 0.5 M H_2SO_4. c) The RRDE voltammetric response of NDCN-22-800/-900/-1000 in O_2-saturated 0.5 M H_2SO_4. d) Polarization curves for the NDCN-22-900 catalyst before and after 4000 potential cycles in O_2-saturated 0.5 M H_2SO_4. Potential cycling was carried out between 0.6 and 1.0 V versus a reversible hydrogen electrode (RHE) at 50 mV s^{-1}. For all the RDE and RRDE measurements, the catalyst loading was 0.6 mg cm^{-2}, the electrode rotation speed was 1600 rpm, and the scan rate was 10 mV s^{-1}.

potential of catalysts were shifted positively upon increasing pore size, which is in agreement with the trend of their performance under alkaline conditions (Figure 3c). The RRDE polarization curves for NDCN-22 are presented in Figure 4b. NDCN-22 exhibited high catalytic activity with a more positive onset potential (0.72 V) and much higher current density (3.57 mA cm^{-2} at 0.50 V) than those of reported nitrogen-doped graphene and nanostructured carbon catalysts.[18] Moreover, NDCN-22 exhibited an ORR process involving almost a 4-electron transfer pathway (n = 3.67–3.91 over the potential 0.03–0.63 V, Figure S7c) with a low H_2O_2 yield of 4.3–16.5% over the measured potential range (inset of Figure 4b).

As the pyrolysis temperature plays an essential role in the formation of active sites for metal-free carbon catalysts, the activity of NDCN-22 was examined for the samples obtained at 800, 900, and 1000 °C (denoted as NDCN-22-800, NDCN-22-900, and NDCN-22-1000, respectively). The activity in acidic medium (0.5 M H_2SO_4), as measured by the ORR onset and half-wave potentials ($E_{1/2}$) in the RRDE polarization curves (Figure 4c), increased from 0.67 and 0.50 V for NDCN-22-800 to 0.72 and 0.56 V for NDCN-22-900. The performance of NDCN-22-1000 is very similar to that of NDCN-22-900. In association with an XPS analysis (Figure S8), the atomic ratio of the graphitic to the pyridinic N atoms (Table S4) is assumed to be responsible for the considerable activity enhancement of NDCN-22-900/-1000 relative to NDCN-22-800.[3c] The high cycling stability of the NDCN-22-900 catalyst is also demonstrated in Figure 4d. The cycling was carried out with CV within a potential range of 0.6–1.0 V in O_2-saturated 0.5 M H_2SO_4.[3a,12a] After 4000 continuous cycles, the half-wave potential $E_{1/2}$ exhibited a small negative shift of about 40 mV under O_2, validating the high durability of the NDCN catalysts.

In summary, we have developed mesoporous nitrogen-doped carbon nanosheets using a template approach. The unique planar porous shells afford abundant catalytic sites on the surface of the NDCN and facilitate the electrolyte/reactant diffusion during the oxygen reduction process. The NDCN catalyst with a pore size of 22 nm exhibits a more positive ORR onset potential than that of Pt/C and a high diffusion-limited current approaching that of Pt/C in alkaline medium. Moreover, the catalyst shows pronounced electrocatalytic activity and long-term stability towards the ORR under acidic conditions. The synthetic strategy toward porous carbon nanosheets described in this work appears to boost the electrocatalytic activity of metal-free catalysts by a controlled mesoporosity, and can be further extended to develop porous nonprecious metal catalysts for high-performance oxygen reduction reactions.

Received: August 20, 2013

Keywords: graphene · mesoporous materials · metal-free catalysts · nitrogen doping · oxygen reduction reaction

[1] a) B. C. Steele, A. Heinzel, *Nature* **2001**, *414*, 345–352; b) E. M. Erickson, M. S. Thorum, R. Vasic, N. S. Marinkovic, A. I. Frenkel, A. A. Gewirth, R. G. Nuzzo, *J. Am. Chem. Soc.* **2012**, *134*, 197–200.

[2] J. Snyder, T. Fujita, M. W. Chen, J. Eelebancher, *Nat. Mater.* **2010**, *9*, 904–907.

[3] a) G. Wu, K. L. More, C. M. Johnston, P. Zelenay, *Science* **2011**, *332*, 443–447; b) Z. S. Wu, S. B. Yang, Y. Sun, K. Parvez, X. F. Feng, K. Müllen, *J. Am. Chem. Soc.* **2012**, *134*, 9082–9085; c) K.

Parvez, S. B. Yang, Y. Hernandez, A. Winter, A. Turchanin, X. F. Feng, K. Müllen, *ACS Nano* **2012**, *6*, 9541 – 9550.

[4] a) K. P. Gong, F. Du, Z. H. Xia, M. Durstock, L. M. Dai, *Science* **2009**, *323*, 760 – 764; b) L. J. Yang, S. J. Jiang, Y. Zhao, L. Zhu, S. Chen, X. Z. Wang, Q. Wu, J. Ma, Y. W. Ma, Z. Hu, *Angew. Chem.* **2011**, *123*, 7270 – 7273; *Angew. Chem. Int. Ed.* **2011**, *50*, 7132 – 7135; c) Z. Yang, Z. Yao, G. F. Li, G. Y. Fang, H. G. Nie, Z. Liu, X. M. Zhou, X. A. Chen, S. M. Huang, *ACS Nano* **2012**, *6*, 205 – 211.

[5] a) D. S. Yu, E. Nagelli, F. Du, L. M. Dai, *J. Phys. Chem. Lett.* **2010**, *1*, 2165 – 2173; b) N. Ramaswamy, S. Mukerjee, *Adv. Phys. Chem.* **2012**, 491604.

[6] a) W. Yang, T. P. Fellinger, M. Antonietti, *J. Am. Chem. Soc.* **2011**, *133*, 206 – 209; b) R. L. Liu, D. Q. Wu, X. L. Feng, K. Müllen, *Angew. Chem.* **2010**, *122*, 2619 – 2623; *Angew. Chem. Int. Ed.* **2010**, *49*, 2565 – 2569; c) S. B. Yang, X. L. Feng, X. C. Wang, K. Müllen, *Angew. Chem.* **2011**, *123*, 5451 – 5455; *Angew. Chem. Int. Ed.* **2011**, *50*, 5339 – 5343; d) L. T. Qu, Y. Liu, J. B. Baek, L. M. Dai, *ACS Nano* **2010**, *4*, 1321 – 1326; e) D. S. Yu, Q. Zhang, L. M. Dai, *J. Am. Chem. Soc.* **2010**, *132*, 15127 – 15129.

[7] a) T. Ikeda, M. Boero, S. F. Huang, K. Terakura, M. Oshima, J. Ozaki, *J. Phys. Chem. C* **2008**, *112*, 14706 – 14709; b) H. Kim, K. Lee, S. I. Woo, Y. Jung, *Phys. Chem. Chem. Phys.* **2011**, *13*, 17505 – 17510; c) C. V. Rao, C. R. Cabrera, Y. Ishikawa, *J. Phys. Chem. Lett.* **2010**, *1*, 2622 – 2627.

[8] a) J. Liang, Y. Jiao, M. Jaroniec, S. Z. Qiao, *Angew. Chem.* **2012**, *124*, 11664 – 11668; *Angew. Chem. Int. Ed.* **2012**, *51*, 11496 – 11500; b) Z. W. Liu, F. Peng, H. J. Wang, H. Yu, W. X. Zheng, J. Yang, *Angew. Chem.* **2011**, *123*, 3315 – 3319; *Angew. Chem. Int. Ed.* **2011**, *50*, 3257 – 3261.

[9] a) L. F. Lai, J. R. Potts, D. Zhan, L. Wang, C. K. Poh, C. H. Tang, H. Gong, Z. X. Shen, J. Y. Lin, R. S. Ruoff, *Energy Environ. Sci.* **2012**, *5*, 7936 – 7942; b) X. Q. Wang, J. S. Lee, Q. Zhu, J. Liu, Y. Wang, S. Dai, *Chem. Mater.* **2010**, *22*, 2178 – 2180; c) C. H. Choi, S. H. Park, S. I. Woo, *ACS Nano* **2012**, *6*, 7084 – 7091.

[10] a) A. K. Geim, K. S. Novoselov, *Nat. Mater.* **2007**, *6*, 183 – 191; b) A. Fasolino, J. H. Los, M. I. Katsnelson, *Nat. Mater.* **2007**, *6*, 858 – 861.

[11] a) Y. Zhao, C. G. Hu, Y. Hu, H. H. Cheng, G. Q. Shi, L. T. Qu, *Angew. Chem.* **2012**, *124*, 11533 – 11537; *Angew. Chem. Int. Ed.* **2012**, *51*, 11371 – 11375; b) I. Y. Jeon, H. J. Choi, M. Choi, J. M. Seo, S. M. Jung, M. J. Kim, S. Zhang, L. P. Zhang, Z. H. Xia, L. M. Dai, N. Park, J. B. Baek, *Sci. Rep.* **2013**, *50*, 1810 – 1817.

[12] a) Y. G. Li, W. Zhou, H. L. Wang, L. M. Xie, Y. Y. Liang, F. Wei, J. C. Idrobo, S. J. Pennycook, H. J. Dai, *Nat. Nanotechnol.* **2012**, *7*, 394 – 400; b) W. Xiong, F. Du, Y. Liu, A. Perez, Jr., M. Supp, T. S. Ramakrishnan, L. M. Dai, L. Jiang, *J. Am. Chem. Soc.* **2010**, *132*, 15839 – 15841; c) C. Jin, T. C. Nagaiah, W. Xia, B. Spliethoff, S. S. Wang, M. Bron, W. Schuhmann, M. Muhler, *Nanoscale* **2010**, *2*, 981 – 987.

[13] S. B. Yang, X. L. Feng, L. Wang, K. Tang, J. Maier, K. Müllen, *Angew. Chem.* **2010**, *122*, 4905 – 4909; *Angew. Chem. Int. Ed.* **2010**, *49*, 4795 – 4799.

[14] R. J. Li, K. Parvez, F. Hinkel, X. L. Feng, K. Müllen, *Angew. Chem.* **2013**, *125*, 5645 – 5648; *Angew. Chem. Int. Ed.* **2013**, *52*, 5535 – 5538.

[15] Z. B. Lei, N. Christov, X. S. Zhao, *Energy Environ. Sci.* **2011**, *4*, 1866 – 1873.

[16] X. D. Huang, K. Qian, J. Yang, J. Zhang, L. Li, C. Z. Yu, D. Y. Zhao, *Adv. Mater.* **2012**, *24*, 4419 – 4423.

[17] K. L. Ai, Y. L. Liu, C. P. Ruan, L. H. Lu, G. Q. Lu, *Adv. Mater.* **2013**, *25*, 998 – 1003.

[18] a) M. Chisaka, T. Iijima, A. Tomita, T. Yaguchi, Y. Sakurai, *J. Electrochem. Soc.* **2010**, *157*, B1701 – B1706; b) D. S. Geng, H. Liu, Y. G. Chen, R. Y. Li, X. L. Sun, S. Y. Ye, S. Knights, *J. Power Sources* **2011**, *196*, 1795 – 1801; c) S. Kundu, T. C. Nagaiah, W. Xia, Y. M. Wang, S. V. Dommele, J. H. Bitter, M. Santa, G. Grundmeier, M. Bron, W. Schuhmann, M. Muhler, *J. Phys. Chem. C* **2009**, *113*, 14302 – 14310; d) K. Kwon, Y. J. Sa, J. Y. Cheon, S. H. Joo, *Langmuir* **2012**, *28*, 991 – 996.

